

# Revised event rates for extreme and extremely large mass-ratio inspirals

Verónica Vázquez-Aceves,<sup>1</sup> Lorenz Zwick,<sup>2</sup> Elisa Bortolas,<sup>3,4</sup> Pedro R. Capelo,<sup>2</sup>

Pau Amaro Seoane,<sup>5,6,7,1</sup> Lucio Mayer<sup>2</sup> and Xian Chen<sup>8,7\*</sup>

<sup>1</sup>*Institute of Applied Mathematics, Academy of Mathematics and Systems Science, Chinese Academy of Sciences, 100190 Beijing, China*

<sup>2</sup>*Center for Theoretical Astrophysics and Cosmology, Institute for Computational Science, University of Zurich, Winterthurerstrasse 190, CH-8057 Zürich, Switzerland*

<sup>3</sup>*Dipartimento di Fisica “G. Occhialini”, Università degli Studi di Milano-Bicocca, Piazza della Scienza 3, I-20126 Milano, Italy*

<sup>4</sup>*INFN, Sezione di Milano-Bicocca, Piazza della Scienza 3, I-20126 Milano, Italy*

<sup>5</sup>*Institute of Multidisciplinary Mathematics, Universitat Politècnica de València, Spain*

<sup>6</sup>*DESY Zeuthen, Germany*

<sup>7</sup>*Kavli Institute for Astronomy and Astrophysics at Peking University, 100871 Beijing, China*

<sup>8</sup>*Department of Astronomy, School of Physics, Peking University, 100871 Beijing, China*

Accepted XXX. Received YYY; in original form ZZZ

## ABSTRACT

One of the main targets of the Laser Interferometer Space Antenna (LISA) is the detection of extreme mass-ratio inspirals (EMRIs) and extremely large mass-ratio inspirals (X-MRIs). Their orbits are expected to be highly eccentric and relativistic when entering the LISA band. Under these circumstances, the inspiral time-scale given by Peters’ formula loses precision and the shift of the last-stable orbit (LSO) caused by the massive black hole spin could influence the event rates estimate. We re-derive EMRIs and X-MRIs event rates by implementing two different versions of a Kerr loss-cone angle that includes the shift in the LSO, and a corrected version of Peters’ time-scale that accounts for eccentricity evolution, 1.5 post-Newtonian hereditary fluxes, and spin-orbit coupling. The main findings of our study are summarized as follows: (1) implementing a Kerr loss-cone changes the event rates by a factor ranging between 0.9 and 1.1; (2) by employing the usual definition of the loss-cone and the corrected version of Peters’ time-scale, we obtain event rates of about 8 to 30 times lower than the rates calculated with the usual Peters’ formula; (3) if we use an alternative version of the gravitational-wave merger time-scale, suitable for high eccentricities, the rates differ from the corrected values by a factor between 0.9 and 3.

**Key words:** black hole physics – gravitational waves – methods: analytical.

## 1 INTRODUCTION

Massive black holes (MBHs) at the centre of galaxies can capture compact objects – such as stellar-mass BHs, white dwarfs (WDs), neutron stars (NSs), and even brown dwarfs (BDs) – that can either suffer a direct plunge or slowly inspiral to the event horizon without being disrupted. The latter events are known as extreme mass-ratio inspirals (EMRIs) when the mass ratio  $q$  between the compact object and the MBH is of the order of  $10^{-4}$ , and as extremely large mass-ratio inspirals (X-MRIs) when  $q \sim 10^{-8}$ . During the inspiral process, the binary would emit low-frequency gravitational waves (GWs) that space-borne detectors like the Laser Interferometer Space Antenna (LISA) can detect (Barack & Cutler 2004; Amaro-Seoane et al. 2012; Klein et al. 2016; Babak et al. 2017; Amaro-Seoane 2018; Barack et al. 2019), providing detailed information about the binary and the surrounding space-time that is impossible to obtain via electro-

magnetic observations. Such detections would allow testing general relativity with exceptional accuracy; therefore, it is crucial to accurately estimate the event rates and the characteristics of inspiral processes.

The eccentricity of an EMRI or X-MRI when entering the LISA band depends on the formation channel. There are two basic formation scenarios that result in two different eccentricity regimes: the two body relaxation driven decay and the so-called Hills mechanism.

The first scenario involves a dynamical process in which two-body relaxation increases the eccentricity of an orbiting object such that, at the pericentre, the object passes so close to the MBH that the energy loss by GW emission becomes significant. Ideally, after a pericentre passage, the orbital parameters evolve exclusively by GW emission, resulting in a very eccentric EMRI or X-MRI in which the semimajor axis can be very large compared to the pericentre. However, the process is not that simple. Relativistic effects can become relevant at pericentre. Moreover, at the apocentre, the two-body relaxation process that initially brought the object into

\* Corresponding author: xian.chen@pku.edu.cn

the desired orbit could either enlarge the pericentre, making the GW emission negligible, or deflect the object into the loss cone where the secondary object rapidly plunges into the MBH and is lost to the system after a single GW burst (Alexander & Hopman 2003). The loss cone is a region of phase space such that the angular momentum of the incoming object is not large enough to escape the MBH (Merritt 2013); it is defined by an angle  $\hat{\theta}_{\text{lc}}$ , known as the loss-cone angle, and depends on the position of the last stable orbit (LSO). For a successful inspiral, the compact object has to be “immune” to relaxation processes once it has reached a pericentre that is sufficiently close to the MBH to emit GWs, i.e. its merger time-scale ( $T_{\text{GW}}$ ) has to be shorter than or similar to the time needed by two-body relaxation to perturb its pericentre. This condition is fulfilled at a specific critical semimajor axis ( $a_{\text{crit}}$ ) that depends on several factors like the mass and spin of the MBH, the distribution of stars and compact objects around it, and the merger time-scale. The value of the critical semimajor axis is necessary to estimate event rates (Sigurdsson & Rees 1997; Hopman & Alexander 2005; Amaro-Seoane et al. 2007).

The second scenario involves a binary system composed of at least one compact object orbiting at short distances from the MBH. If the gravitational force from the MBH acting on one of the binary components is larger than the binding energy, the binary is disrupted and one of the objects is captured by the MBH. If the captured object is a compact object, it could become an EMRI or X-MRI, as it can resist tidal disruption at such close distances. Its initial semimajor axis would be equal to the binary-disruption distance, which is smaller than the semimajor axis involved in the two-body relaxation formation process. As a result, the eccentricity of an EMRI or X-MRI formed by this process would be low when it enters the LISA band (Amaro-Seoane 2020). This idea is based on the work of Hills (1988), who predicted that the presence of an MBH in the Galactic centre would result in the disruption of binary systems composed of main-sequence stars: one of the stars would be tidally disrupted, while the other would be ejected at high velocities (up to  $v > 4 \times 10^3 \text{ km s}^{-1}$ ). These “hyper-velocity stars” were first discovered by Brown et al. (2005), who detected a star leaving the Galaxy with velocity  $\sim 700 \text{ km s}^{-1}$ , providing evidence of the existence of the process. However, the population of binary systems containing compact objects near an MBH is not well understood, impeding reliable event-rate estimations.

In this work, we obtain event rates ( $\dot{\Gamma}_i$ ) of EMRIs and X-MRIs formed by two-body relaxation around Schwarzschild (1916) and Kerr (1963) MBHs with a mass similar to that of Sgr A\* ( $4.3 \times 10^6 M_{\odot}$ ), by modifying two elements: the merger (or inspiral) time-scale and the loss-cone angle  $\hat{\theta}_{\text{lc}}$ .

Usually, the merger time-scale of a binary system is obtained with Peters’ formula (Peters & Mathews 1963; Peters 1964). However, in this formation scenario, the high eccentricities and the relativistic effects that appear in the proximity of the MBH reduce the accuracy of Peters’ approach. In Section 2, we describe a set of correction factors presented by Zwick et al. (2020, 2021) that improve Peters’ time-scale behavior under such circumstances, and compare it with an alternative form of Peters’ formula, valid for high eccentricities, previously used to obtain EMRI and X-MRI

event rates (Hopman & Alexander 2005; Amaro-Seoane et al. 2013; Amaro-Seoane 2019).

The critical semimajor axis and the loss cone depend on the position of the LSO, which is constant for a non-spinning MBH and is defined through the Schwarzschild radius ( $r_s$ ), but for a Kerr MBH it also depends on the spin magnitude and on the orbital inclination of the secondary object. Amaro-Seoane et al. (2013) obtained event rates that account for this effect and found that objects originally classified as direct plunges can form an EMRI if they approach in prograde orbits, whereas objects in retrograde orbits contribute more to the plunge rate. In Section 3, we re-derive the critical semimajor axis for Schwarzschild and Kerr MBHs including the correction factors in the merger time-scale and the shift in the LSO. In Section 4, we present the necessary elements to estimate the event rates, and we derive two versions of a Kerr loss-cone angle that account for the shift in the LSO position to finally obtain an expression for  $\dot{\Gamma}_i$  that includes the Peters’ time-scale corrections and the Kerr loss-cone angle.

In Section 5, we analyze the effects of the time-scale correction factors and the Kerr loss-cone angle on the event rates for EMRIs and X-MRIs composed of stellar-mass BHs, NSs, WDs, and BDs. We consider prograde and retrograde orbits with orbital inclinations  $|\theta| = [0, 0.1, 0.4, 0.7, 1.0, 1.3, 1.57]$  radians, and an MBH with dimensionless spin  $a_{\bullet} = 0$  to  $a_{\bullet} = 0.999$ .<sup>1</sup> Finally, we conclude in Section 6.

## 2 THE INSPIRAL TIME-SCALE

A reliable estimate of the merger time-scale is needed to understand the inspiral processes. In this work, we refer to a generic GW-induced decay time-scale as  $T_{\text{GW}}$ . The most commonly used estimate of  $T_{\text{GW}}$  is the so-called Peters’ formula,

$$T_{\text{P}}(a_0, e_0) = \frac{5}{256} \frac{a_0^4 c^5}{G^3 M_{\text{MBH}} m_2 (M_{\text{MBH}} + m_2)} f(e_0), \quad (1)$$

where  $a_0$  and  $e_0$  are the initial semimajor axis and eccentricity, respectively,  $m_2$  is the mass of the orbiting compact object, and

$$f(e_0) = (1 - e_0^2)^{7/2} \left( 1 + \frac{73}{24} e_0^2 + \frac{37}{96} e_0^4 \right)^{-1}. \quad (2)$$

This formula was obtained by Peters (1964) based on the following assumptions:

- (A) The binary’s orbit is Keplerian.
- (B) GW radiation is described by Einstein (1916)’s quadrupole formula.
- (C) The secular evolution of the orbital parameters is slow with respect to the period of the orbit.
- (D) The secular evolution of the eccentricity can be neglected.

Because of these assumptions, Peters’ formula is not an

<sup>1</sup> We define the MBH spin as  $a_{\bullet} = cJ_{\text{MBH}}/(GM_{\text{MBH}}^2)$ , where  $M_{\text{MBH}}$  and  $J_{\text{MBH}}$  are the MBH’s mass and angular momentum magnitude, respectively,  $c$  is the speed of light in vacuum, and  $G$  is the gravitational constant.

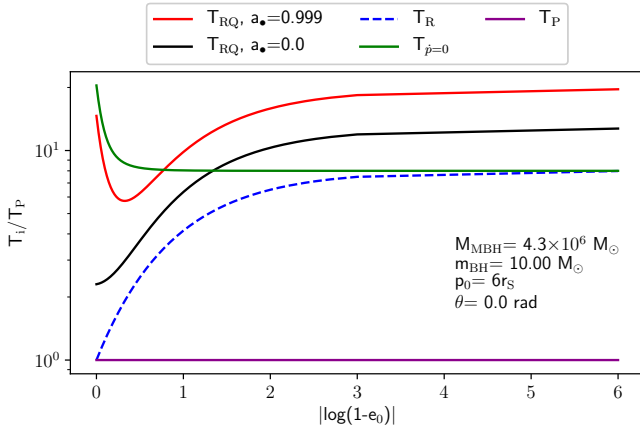


**Figure 1.** Comparison between the different merger time-scales normalized to the Peters’ time-scale  $T_P$  (purple solid line), for the case of a compact object of  $10 M_\odot$  in an equatorial prograde orbit around a  $4.3 \times 10^6 M_\odot$  MBH, with  $p_0 = 6r_S$ . The green solid line,  $T_{\dot{p}=0}$ , is the time-scale obtained with Equation (3). The blue dashed line,  $T_R$ , includes the correction for the secular eccentricity evolution  $R$  (Equation 4). The black ( $a_\bullet = 0$ ) and red ( $a_\bullet = 0.999$ ) solid lines,  $T_{RQ}$ , include the correction factors  $R$  and  $Q$ , which accounts for post-Newtonian effects up to order 1.5.

exact measure of  $T_{\text{GW}}$ , and fails to accurately model the behavior of highly eccentric and highly relativistic orbits.

The case of highly eccentric orbits ( $e_0 > 0.9$ ) is important for EMRI and X-MRI event rates estimates. Therefore, some authors (e.g. Hopman & Alexander 2005; Amaro-Seoane et al. 2013; Amaro-Seoane 2019) adopted a different estimate for  $T_{\text{GW}}$ , which is purpose-built to describe highly eccentric orbits more accurately. It is obtained by modifying assumption (D) to

(D\*) The secular evolution of the pericentre can be neglected.

Assumption (D\*) is much better suited to describe orbits with extreme eccentricities for which the pericentre remains nearly constant during the inspiral. The resulting time-scale is then given by

$$T_{\dot{p}=0}(a_0, e_0) \simeq \sqrt{2} \frac{24}{85} \frac{a_0^4 c^5}{G^3 m_2 M_{\text{MBH}}^2} (1 - e_0)^{7/2}. \quad (3)$$

The two time-scales presented above (Equations 1 and 3) differ in their range of validity because of their different assumptions.

In Zwick et al. (2020), a simple correction factor,  $R$ , is proposed to correct for the omitted secular eccentricity evolution, and therefore it interpolates between the low-eccentricity validity of  $T_P$  and the high-eccentricity validity of  $T_{\dot{p}=0}$  (see also Bonetti et al. 2018, for an alternative formulation). The correction factor is

$$R(e_0) = 8^{1 - \sqrt{1 - e_0}}. \quad (4)$$

By multiplying  $T_P$  by  $R$ , Peters’ formula extends its validity to all eccentricities. The corrected formula, denoted as  $T_R$ , reproduces  $T_{\dot{p}=0}$  in the high-eccentricity limit. The time-scale  $T_R$  effectively does away with assumption (D) or (D\*).

Zwick et al. (2021) obtained an additional correction factor  $Q$  that improves the estimate of the inspiral time-scale by

Name	Validity	Time-scale accuracy	PN effects
$T_P$	Low $e_0$	underestimates	No
$T_{\dot{p}=0}$	High $e_0$	over/under	No
$T_R$	Any $e_0$	underestimates	No
$T_{RQ}$	Any $e_0$	best	Yes

**Table 1.** In this table we summarize the characteristics and validity ranges of the different estimates for the GW-induced merger time-scales. We use the corrected time-scale  $T_{RQ}$  as a benchmark from which to say whether the time-scales  $T_{\dot{p}=0}$ ,  $T_P$ , and  $T_R$  over or underestimate the result.

modelling post-Newtonian effects up to order 1.5, based on the following assumptions:

- (A\*) The binary’s orbit is post-Newtonian (1 PN).
- (B\*) GW radiation is described by post-Newtonian fluxes (1.5 relative PN).
- (C) The secular evolution of the orbital parameters is slow with respect to the period of the orbit.

The common theme among all of these formulations is assumption (C), which is appropriate when the mass ratio of the binary is extreme and the residence time at a given separation,  $a/\dot{a} \propto 1/q$ , is much longer than the period of an orbit.

The explicit formula of  $Q$  is found in Zwick et al. (2021); this correction factor is valid for arbitrary values of initial eccentricity, semimajor axis, MBH spin, and orbital inclination  $\theta$ . The fully corrected time-scale is

$$T_{RQ} = T_P R Q. \quad (5)$$

Equation (5) takes into account the relativistic effects that can influence the inspiral resulting in an accurate time-scale for the eccentricity regime ( $e_0 > 0.9$ ) and pericentre distances ( $p_0 \lesssim 6r_S$ ) expected for EMRIs and X-MRIs.

Figure 1 shows the differences between the various GW-induced merger time-scales as a function of eccentricity for a BH of  $10 M_\odot$  in an equatorial prograde orbit (with  $p_0 = 6r_S$ ) around a Milky Way-like MBH, with  $M_{\text{MBH}} = 4.3 \times 10^6 M_\odot$  and  $a_\bullet = 0$  or  $a_\bullet = 0.999$ . Note that, in the limit of high eccentricity,  $T_P \rightarrow T_{\dot{p}=0}/8$  and  $T_{\dot{p}=0}$  is  $\sim 60$  ( $\sim 40$ ) per cent of  $T_{RQ}$  when  $a_\bullet = 0$  ( $a_\bullet = 0.999$ ). An interesting coincidence occurs when the correction factors  $R$  and  $Q$  multiplied together mimic the factor of  $\sim 8$  difference between  $T_P$  and  $T_{\dot{p}=0}$  and the two lines ( $T_{RQ}$  and  $T_{\dot{p}=0}$ ) cross over each other. For equatorial orbits, this effect occurs at  $e_0 \sim 0.8$  if  $a_\bullet = 0.999$  and at  $e_0 \sim 0.95$  if  $a_\bullet = 0$ .

Peters’ time-scale  $T_P$  underestimates the merger time since it assumes that the eccentricity remains at its initial value throughout the evolution, artificially boosting the radiation of GWs. In contrast, the time-scale  $T_{\dot{p}=0}$  overestimates the merger time-scale for low eccentricities since it assumes that the pericentre of the orbit does not decay, artificially decreasing the amount of GW emitted. The effect of the PN correction factors is to increase the estimate of the merger time-scale, especially for circular orbits. Nevertheless, for  $p_0 \lesssim 6r_S$  and eccentricity values  $e_0 > 0.9$ , relevant for EMRIs and X-MRIs,  $T_{\dot{p}=0} \in (1.2 - 0.4) \times T_{RQ}$ . Table 1 summarizes the characteristics of the different merger time-scales.

### 3 THE CRITICAL SEMIMAJOR AXIS

The critical semimajor axis  $a_{\text{crit}}$  marks the end of the relaxation-driven evolution regime, i.e. two-body relaxation effects become irrelevant, and the energy loss due to GWs emission dominates the evolution of the orbit. Its value is found by solving

$$T_{\text{GW}} = T_{\text{peri}}(a_0, e_0), \quad (6)$$

where  $T_{\text{GW}}$  is the merger time-scale, and  $T_{\text{peri}}$  is the time required by two-body relaxation to change the pericentre of the inspiraling object (Amaro-Seoane et al. 2007), given by

$$T_{\text{peri}}(a_0, e_0) = T_{\text{rlx}}(a_0) \times (1 - e_0^2). \quad (7)$$

This time-scale is derived from the angular momentum diffusion time-scale,

$$T_{\text{J}} \sim T_{\text{rlx}} \times [J/J_{\text{max}}]^2 = T_{\text{rlx}}(a)(1 - e_0^2), \quad (8)$$

where  $J = (a(1 - e^2)GM_{\text{MBH}})^{1/2}$ ,  $J_{\text{max}} = (aGM_{\text{MBH}})^{1/2}$  is the angular momentum of a circular orbit, and  $T_{\text{rlx}}(a)$  is the relaxation time-scale at a distance equal to the semimajor axis  $a$  (see Equation 10 below).

Two-body interactions also cause energy diffusion, which changes the semimajor axis of the objects orbiting the MBH on the relaxation time-scale

$$T_{\text{rlx}} \sim \mathcal{E}/\dot{\mathcal{E}}, \quad (9)$$

where  $\mathcal{E} = GM_{\text{MBH}}/2a$ . This effect is not relevant to the inspiral process because, only by energy diffusion, it can take several relaxation time-scales to reach orbital parameters for which GWs emission becomes significant. From Equation (8), if  $e_0 \neq 0$ , then  $T_{\text{J}} \lesssim T_{\text{rlx}}$ , indicating that two-body relaxation diffuses angular momentum faster than it diffuses energy (Hopman & Alexander 2005), increasing the eccentricity of an orbit while its semimajor axis remains approximately constant, allowing the object to reach very short distances to the MBH at the pericentre. This is a key dynamical aspect in the EMRIs/X-MRIs formation; taking  $T_{\text{peri}}(a_0, e_0) = T_{\text{J}}$  in Equation (6) guarantees that objects with  $a_0 \lesssim a_{\text{crit}}$  that reached highly eccentric orbits due to a decrease in their angular momentum, merge before their pericentre changes by diffusion. If the term  $(1 - e_0^2)$  is omitted in the same equation, systems with longer  $T_{\text{GW}}$  for which diffusion in angular momentum is still significant can be mistakenly considered as potential inspiraling sources, artificially increasing the event rates.

The next step in describing the EMRI/X-MRI formation is to set a condition for the pericentre of an inspiraling orbit. At each pericentre passage, the energy loss by GWs emission is maximum and the semimajor axis shrinks, increasing the binding energy between the MBH and the compact object. If the new binding energy is high enough, the binary decouples dynamically from the surrounding stellar system, and diffusion in  $J$  and  $\mathcal{E}$  becomes negligible. The orbit then evolves only due to the energy loss by GWs emission, creating a successful inspiral that ends when the object crosses the event horizon of the central MBH.

We fix the pericentre at the LSO around the MBH. This

condition sets a limit for the eccentricity of a non-plunging orbit given by  $e_{\text{plunge}} = 1 - r_{\text{LSO}}/a_0$ , with  $r_{\text{LSO}}$  the LSO position. If  $e_0 > e_{\text{plunge}}$ , the pericentre of the orbit is located inside the LSO and the object is sent to the event horizon of the MBH after a single pericentre passage (Amaro-Seoane et al. 2007). The pericentre of an orbit with  $e_0 \lesssim e_{\text{plunge}}$  is located at the closest possible distance to the MBH such that an object  $m_2$  becomes immune to relaxation process, remains in a stable orbit, radiates away a significant amount of GWs at  $p_0$ , and continues inspiraling into the MBH for a large number of cycles before the merger.

Similarly,  $a_{\text{crit}}$  defines whether a given source is likely to become an inspiral or remains in the dynamical regime by setting a limit on the energy. If  $\mathcal{E}_{\text{source}} < \mathcal{E}_{\text{crit}}$ , the object is too far away from the MBH to become an inspiral and remains in the dynamical regime; it performs a random walk in the phase space driven by diffusion in energy and angular momentum, to finally either plunge into the MBH, diffuse to wider orbits, or become a potential inspiral source by diffusing into tighter orbits. These scenarios are characterized by the balance between  $T_{\text{peri}}$  and the GW time-scale  $T_{\text{GW}}$ . While the latter depends only on the source characteristics, the former requires a model of the stellar density in the vicinity of the MBH.

To estimate  $T_{\text{rlx}}$ , we consider that inside the influence radius of the MBH, defined as  $R_{\text{h}} = GM_{\text{MBH}}/\sigma_0^2$ , with  $\sigma_0$  the central velocity dispersion, the stellar density distribution follows a power-law cusp  $\rho(r) \sim r^{-\gamma}$ . This is a theoretical prediction of Peebles (1972) and Bahcall & Wolf (1976) from the 1970s that has been tested in the past decade by numerical approaches (see, e.g. Freitag & Benz 2001; Amaro-Seoane et al. 2004; Preto & Amaro-Seoane 2009), concluding that stellar cusps may be common around MBHs. A strong support of these assumptions is found in the work of Gallego-Cano et al. (2018); Schödel et al. (2018); Baumgardt et al. (2018), in which the authors conduct an extensive search for the stellar density cusp around Sgr A\*, by performing observations and  $N$ -body simulations of the innermost structure of the Milky Way’s nuclear star cluster. They find an excellent agreement between the theory, their observational data, and their simulations, consistent with the existence of a power-law density cusp around Sgr A\*.

Stellar-mass BHs dominate the central density as they sink to the centre due to mass segregation forming a cusp for which different indices have been suggested, for example  $\gamma = 1.3$ – $1.4$  (Freitag et al. 2006),  $\gamma = 1.75$  (Bahcall & Wolf 1976), and  $2 \lesssim \gamma \lesssim 11/4$  in strong mass segregation scenarios (Alexander & Hopman 2009; Preto & Amaro-Seoane 2009; Amaro-Seoane & Preto 2011). We assume that these objects with a typical mass of  $m_{\text{BH}} = 10 M_{\odot}$  are the driving species in the relaxation process. Less massive species distribute into a shallower profile and do not affect the relaxation rates.

The relaxation time-scale inside  $R_{\text{h}}$  at a distance equal to the semimajor axis  $a$  (Baumgardt et al. 2004a,b; Freitag & Benz 2002; Hopman & Alexander 2005) is

$$T_{\text{rlx}} = T_0 \left( \frac{a}{R_{\text{h}}} \right)^{\gamma-3/2}, \quad (10)$$

$$T_0 = 0.3389 \frac{\sigma_0^3}{\ln(\Lambda)G^2 m_{\text{BH}}^2 n_0}, \quad (11)$$

where  $\ln(\Lambda) \simeq 13$  is the Coulomb logarithm (Binney & Tremaine 1987), and  $n_0$  is the number density given by

$$n_0 = \frac{3 - \gamma}{4\pi} \frac{N_0}{R_h^3}, \quad (12)$$

$$\sigma_0 = \left( \frac{1}{1 + \gamma} \frac{GM_{\text{MBH}}}{R_h} \right)^{1/2}, \quad (13)$$

where  $N_0$  is the number of stellar-mass BHs inside  $R_h$ . With these elements, Equation (11) becomes

$$T_0 \simeq \frac{4.26}{(3 - \gamma)(1 + \gamma)^{3/2}} \frac{\sqrt{R_h^3 (GM_{\text{MBH}})^{-1}}}{\ln(\Lambda) N_0} \left( \frac{M_{\text{MBH}}}{m_{\text{BH}}} \right)^2. \quad (14)$$

To fix the pericentre, we assume that the LSO for a Schwarzschild MBH is located at  $4r_s$  (Teukolsky & Shapiro 1983). For a Kerr MBH, the change in the position of the LSO due to the spin and inclination with respect to the spin axis, is modelled through the function  $\mathcal{W}(\theta, a_\bullet)$  derived in Amaro-Seoane et al. (2013) from the separatrices between stable and unstable (plunging) orbits. The inclusion of  $\mathcal{W}(\theta, a_\bullet)$  can increase the number of cycles a prograde EMRI or X-MRI spends inside the LISA frequency band in such a way that it becomes detectable. Its derivation is based on the scheme presented in Sopuerta & Yunes (2011), that takes elements from the multipolar, post-Minkowskian formalism and BH perturbation theory to describe an inspiral trajectory, including also the radiation-reaction from the GWs emission to the system. For a Kerr MBH, the effective pericentre at the LSO is

$$p = a(1 - e) = \mathcal{W}(\theta, a_\bullet) \times \frac{8GM_{\text{MBH}}}{c^2}. \quad (15)$$

As inspiral time-scale, we take Equation (5) to include the correction factors, and evaluate it at the LSO as long as it is located no closer than  $3r_s$ . At shorter distances, the correction factors involving the PN terms are not accurate (Zwick et al. 2021); in that case, we compute  $Q$  at  $3r_s$ . We re-write the correction factor  $Q$  in terms of the MBH spin, the function  $\mathcal{W}(\theta, a_\bullet)$ , and the initial eccentricity.

If  $p_0 \leq 3r_s$ , the correction factor  $Q$  is computed at  $3r_s$ :

$$Q = \exp(A) [1.67 - 2.75(e_0^2 - 3.16e_0)], \quad (16)$$

$$A = s \left[ \frac{0.15}{1.5} e_0 + 1.37(1 - e_0)^{3/2} \right] + |s|^{3/2} \left[ (0.36e_0)^{5/2} + 2.94(1 - e_0)^3 \right],$$

where  $s = a_\bullet \cos(\theta)$ .

If  $p_0 > 3r_s$ , the correction factor  $Q$  is given by

$$Q = q_h(e_0, \mathcal{W}(\theta, a_\bullet)) q_s(s, e_0, \mathcal{W}(\theta, a_\bullet)), \quad (17)$$

with

$$q_h(e_0, \mathcal{W}(\theta, a_\bullet)) = \exp\left(\frac{0.7}{\mathcal{W}(\theta, a_\bullet)}\right) \times \left\{ 1 + (1 - e_0)^2 \left[ \exp\left(\frac{0.55}{\mathcal{W}(\theta, a_\bullet)}\right) - 1 \right] + \left(\frac{0.95}{\mathcal{W}(\theta, a_\bullet)}\right)^{3/2} (e_0^2 - e_0) \right\},$$

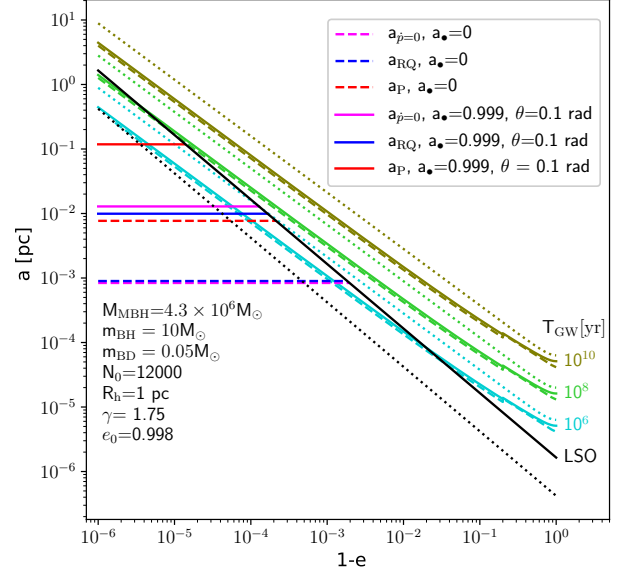


**Figure 2.** Critical semimajor axis as a function of eccentricity, for an inspiraling BD with  $e_0=0.998$ . We consider  $a_\bullet=0$  and  $a_\bullet=0.999$ , for which the orbital inclination of the BD is  $\theta=0.1$  rad. These values of spin and  $\theta$  maximize the correction associated with the spin. The diagonal green colored curves are isochrones that represent the inspiral time of the binary in years. The dotted isochrones are obtained with Peters’ formula (Equation 1), the solid isochrones with the corrected time-scale  $T_{\text{RQ}}$  and  $a_\bullet=0$ , and the dashed isochrones with  $T_{\text{RQ}}$  and  $a_\bullet=0.999$ . Black lines represent the LSO, the solid line is the Schwarzschild case, and the dotted, the Kerr case. The intersection between the LSO and the horizontal lines are the values of  $a_{\text{crit}}$  for the Schwarzschild and Kerr cases. The subscript  $RQ$  (blue lines) indicates that the correction factors in Equation (18) are included, whereas the subscript  $P$  (red lines) indicates the value without the corrections. The magenta lines indicates the value of  $a_{\dot{p}=0}$ , obtained using the merger time-scale  $T_{\dot{p}=0}$ , given by Equation (3).

$$q_s(s, e_0, \mathcal{W}(\theta, a_\bullet)) =$$

$$\exp \left\{ s \left[ \frac{0.3 e_0}{4\mathcal{W}(\theta, a_\bullet)} + (1 - e_0)^{3/2} \left( \frac{3.7}{4\mathcal{W}(\theta, a_\bullet)} \right)^{3/2} \right] + |s|^{3/2} \left[ \left( \frac{0.275 e_0}{\mathcal{W}(\theta, a_\bullet)} \right)^{5/2} + (1 - e_0)^3 \left( \frac{1.075}{\mathcal{W}(\theta, a_\bullet)} \right)^3 \right] \right\}.$$

Combining these elements, the critical semimajor axis takes the form

$$a_{\text{crit}} = R_h \left[ \varepsilon \frac{\mathcal{W}(\theta, a_\bullet)^{5/2}}{m_2(M_{\text{MBH}} + m_2)} \right]^{1/(\gamma-3)} \times \left[ \frac{f(e_0)}{(1 - e_0^2)(1 - e_0)^{5/2}} RQ \right]^{1/(\gamma-3)}, \quad (18)$$

$$\varepsilon = \frac{(3 - \gamma)(1 + \gamma)^{3/2}}{4.26} \left( \frac{5 \times 8^{5/2}}{256} \right) N_0 \ln(\Lambda).$$

The correction factors can be turned off by setting  $RQ = 1$ , in which case  $a_{\text{crit}}$  is determined by  $T_P$  (Equation 1) and is denoted as  $a_P$ . If the correction factors  $RQ$  are applied,

Inspiring object	mass [ $M_{\odot}$ ]	$f_{\text{sub}}$
Stellar-mass BH	10.0	$8.13 \times 10^{-4}$
Neutron star (NS)	2.7	$4.24 \times 10^{-3}$
White dwarf (WD)	0.8	$7.20 \times 10^{-2}$
Brown dwarf (BD)	0.05	0.21

**Table 2.** Mass and fraction number of inspiraling objects.

the critical semimajor axis is denoted as  $a_{\text{RQ}}$ , and as  $a_{\dot{p}=0}$  if its value is derived using  $T_{\dot{p}=0}$  as the merger time-scale (see equation 28 in [Amaro-Seoane 2019](#)).

Figure 2 shows the values of  $a_{\text{RQ}}$ ,  $a_{\text{P}}$ , and  $a_{\dot{p}=0}$  for a BD X-MRI with  $e_0=0.998$  inspiraling into a Schwarzschild MBH, and into a Kerr MBH for which  $a_{\bullet}=0.999$ , and  $\theta=0.1$  rad. For  $a_{\bullet}=0$ , we find that  $a_{\text{P}} \sim 8.5 a_{\text{RQ}}$ , which can significantly reduce the event rates when computed with  $a_{\text{RQ}}$ ; in contrast, the value of  $a_{\dot{p}=0}$  is of about  $0.9 a_{\text{RQ}}$ . In the Kerr case, the effect of  $R$  and  $Q$  is larger resulting in  $a_{\text{P}} \sim 12 a_{\text{RQ}}$ , and  $a_{\dot{p}=0} \sim 1.3 a_{\text{RQ}}$ .

The difference between  $a_{\text{P}}$  and the values obtained for  $a_{\dot{p}=0}$  and  $a_{\text{RQ}}$  originates in the lack of accuracy of Peters' time-scale for highly eccentric and relativistic orbits, revealing the need to thoroughly verify Peters' time-scale's validity depending on the physical characteristics of the system.

#### 4 THE INSPIRAL EVENT RATE

The event rate of successful inspirals is calculated by integrating the number of sources ([Hopman & Alexander 2005](#)),  $n(a)$ , in a volume defined from the minimum distance at which we expect to find at least one potential EMRI/X-MRI source,  $a_{\text{min}}$  ([Amaro-Seoane 2019](#), see Equation 22 below), to the critical semimajor axis:

$$\dot{\Gamma}_{\text{i}} \simeq \int_{a_{\text{min}}}^{a_{\text{crit}}} \frac{dn(a)}{T_{\text{rlx}}(a) \ln(\hat{\theta}_{\text{lc}}^{-2})}, \quad (19)$$

where  $dn(a)$  is obtained from the number of potential sources around the MBH, as explained below, and  $\hat{\theta}_{\text{lc}}$  is the loss-cone angle associated to the position of the LSO.

Inside the integration volume defined by  $a_{\text{min}}$  and  $a_{\text{crit}}$ , two-body relaxation is the leading mechanism that brings a source sufficiently close to the MBH to produce an inspiral event. In the following section, we derive  $a_{\text{min}}$ ,  $dn(a)$ , and the loss-cone angle of a Kerr MBH that can deviate from a Schwarzschild loss-cone angle if the spin of the MBH is sufficiently high.

##### 4.1 Number of sources around a MBH

To obtain the number of objects of a given species, we assume that, similarly to stellar-mass BHs, lighter objects follow a mass density distribution given by a power law with exponent  $\beta$ , resulting in a two-population system in which the value of  $\gamma$  dictates the distribution of the stellar-mass BHs around the MBH, and  $\beta$  the inspiraling object's population distribution. The number of objects of a given species within a given semimajor axis is

$$N(a) = f_{\text{sub}} N_{\text{tot}} \left( \frac{a}{R_{\text{h}}} \right)^{3-\beta}, \quad (20)$$

where  $N_{\text{tot}}$  is the total number of objects (main-sequence stars, compact objects, and substellar objects) within the influence radius of the MBH, and  $f_{\text{sub}}$  is the fraction number of the considered species obtained from a [Kroupa \(2001\)](#) broken power law,  $\Phi(m) \propto m_{\star}^{-\alpha}$ , with  $m_{\star}$  the average stellar mass. We use  $\alpha = [0.3, 1.3, 2.3]$  for the mass intervals  $[0.01, 0.07, 0.5, 150] \times M_{\odot}$  where  $[0.01-0.07] M_{\odot}$  is the BD mass range. Table 2 shows the masses and fraction numbers of each considered object. The numerator of Equation (19) comes from differentiating Equation (20)

$$dn(a) = f_{\text{sub}} (3 - \beta) \frac{N_{\text{tot}}}{R_{\text{h}}} \left( \frac{a}{R_{\text{h}}} \right)^{2-\beta} da. \quad (21)$$

The distance  $a_{\text{min}}$  at which at least one object of a given species can be found is obtained by setting Equation (20) equal to 1 and taking  $N_{\text{tot}} = M_{\text{MBH}}/m_{\star}$ ,

$$a_{\text{min}} = R_{\text{h}} \left( \frac{m_{\star}}{f_{\text{sub}} M_{\text{MBH}}} \right)^{3-\beta}. \quad (22)$$

##### 4.2 The loss-cone angle for Schwarzschild and Kerr black holes

Not all the objects that approach the MBH can produce an EMRI or X-MRI. The pericentre distance has to be sufficiently small for GWs emission to occur; however, if it falls within the LSO, the object suffers a direct plunge. We can identify plunging orbits through their velocity vector; if it lies within a cone defined by a half-angle equal to the loss-cone angle, the orbit takes the object inside a sphere of radius equal to the LSO and rapidly merges with the MBH. The loss-cone angle is calculated as

$$\hat{\theta}_{\text{lc}} = \left( \frac{J_{\text{lc}}^{\text{max}}}{J_{\text{lc}}} \right)^{-1/2}, \quad (23)$$

where  $J_{\text{lc}}^2 = GM_{\text{MBH}} r_{\text{lc}}$  is the angular momentum of an orbit around the MBH that takes a particle to a distance equal to the loss-cone radius  $r_{\text{lc}}$ , defined by the position of the LSO. For a Schwarzschild BH,  $r_{\text{lc,S}} = 4r_{\text{S}}$ , thus the associated loss-cone angle is

$$\hat{\theta}_{\text{S}} = \left( \frac{a}{8r_{\text{S}}} \right)^{-1/4}. \quad (24)$$

For a Kerr BH, the shift in the LSO changes the loss-cone radius; therefore, it is necessary to implement a Kerr loss-cone angle that considers this effect. We implement two versions for the Kerr loss-cone angle; the first, is based on the LSO position shift given by the function  $\mathcal{W}(\theta, a_{\bullet})$ . We write the Kerr loss-cone radius as  $r_{\text{lc,W}} = 4r_{\text{S}} \mathcal{W}(\theta, a_{\bullet})$ ; the associated loss-cone angle is

$$\hat{\theta}_{\text{W}} = \left( \frac{a}{8r_{\text{S}} \mathcal{W}(\theta, a_{\bullet})} \right)^{-1/4} = \hat{\theta}_{\text{S}} \mathcal{W}(\theta, a_{\bullet})^{1/4} \quad (25)$$

For the second version, we use the analytic approximation

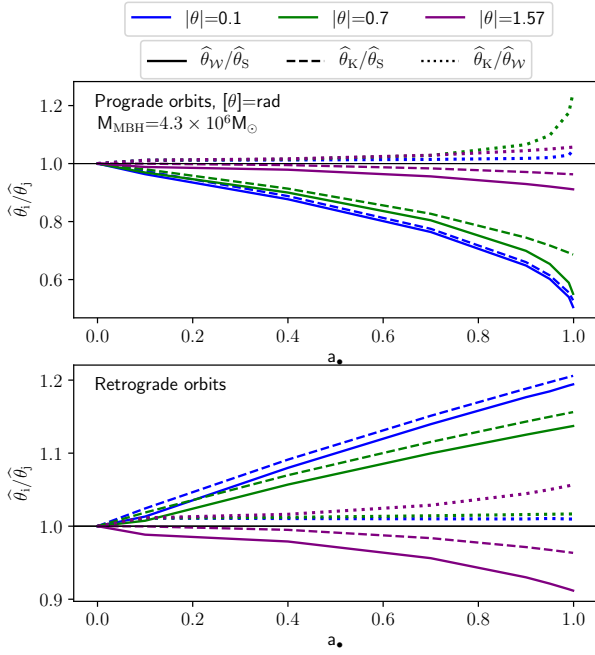


**Figure 3.** The figure shows the ratio between the loss-cone angles  $\hat{\theta}_i/\hat{\theta}_j = [\hat{\theta}_{\mathcal{W}}/\hat{\theta}_S, \hat{\theta}_K/\hat{\theta}_S, \hat{\theta}_K/\hat{\theta}_{\mathcal{W}}]$  obtained with Equations (24), (25), and (27). We show prograde (top panel) and retrograde (bottom panel) orbits with three different orbital inclinations:  $|\theta| = [0.1, 0.7, 1.57]$  rad. The black horizontal line is plotted as a reference: the closer the lines are to the black line, the closer the values are between them. The ratios  $\hat{\theta}_{\mathcal{W}}/\hat{\theta}_S$  and  $\hat{\theta}_K/\hat{\theta}_S$  indicate the deviation of the Kerr loss-cone angle with respect to the Schwarzschild case as a function of the MBH spin, whereas  $\hat{\theta}_K/\hat{\theta}_{\mathcal{W}}$  shows the difference between the two versions of the Kerr loss-cone angle.

for the critical angular momentum ( $J_{\text{crit}}$ ) of a non-relativistic test particle orbiting a Kerr BH obtained by Will (2012), which compared to numerical solutions is accurate within a 5 per cent for  $0.9 \leq a_{\bullet} \leq 0.99$ , and is valid for arbitrary orbital inclinations:

$$J_{\text{crit}} = \frac{GM}{c} [2K(\theta, a_{\bullet}) + 2], \quad (26)$$

$$K(\theta, a_{\bullet}) = \sqrt{1 - s - (1/8)a_{\bullet}^2 \sin^2(\theta) F(a_{\bullet}, \cos(\theta))},$$

$$F(a_{\bullet}, \cos(\theta)) = 1 + \frac{s}{2} + \frac{a_{\bullet}^2}{64} (7 + 13 \cos^2(\theta)) + \frac{a_{\bullet}^2 s}{128} (23 + 5 \cos^2(\theta)) + \frac{a_{\bullet}^4}{2048} (55 + 340 \cos^2(\theta) - 59 \cos^4(\theta)) + \mathcal{O}^5(a_{\bullet}^5).$$

A particle with  $J < J_{\text{crit}}$  rapidly plunges into the MBH, determining a Kerr loss-cone angle given by

$$\hat{\theta}_K = \left( \frac{2a}{r_S} [2K(\theta, a_{\bullet}) + 2]^{-2} \right)^{-1/4}. \quad (27)$$

An inspiraling object approaching an MBH in a prograde orbit finds the LSO closer to the MBH; consequently, the loss-cone angle magnitude decreases with respect to the Schwarzschild case, and it is easier for the incoming body to

avoid direct plunge. For retrograde orbits, the LSO is pushed away from the MBH; hence the loss-cone angle magnitude is larger than in the prograde cases, increasing the phase space that produces a direct plunge. This effect can be easily seen in Equation (25) as  $\mathcal{W}(\theta, a_{\bullet}) \lesssim 1$  for prograde orbits, and  $\gtrsim 1$  for the retrograde cases.

In Figure 3, we show that the two versions of the Kerr loss-cone angle yield similar results, especially for retrograde orbits with  $\theta \lesssim -1.3$  rad. The value of  $\hat{\theta}_K$  slightly deviates from  $\hat{\theta}_{\mathcal{W}}$  in the case of prograde orbits with  $\theta \sim 0.4$ – $0.7$  rad and  $a_{\bullet} \gtrsim 0.95$ .

The MBH spin effects are weak for  $\theta \sim \pm 1.57$  rad, and both versions of the Kerr loss-cone angle indicates that if the inspiraling object approaches an MBH in a highly inclined orbit, regardless if it is in a prograde or retrograde orbit, the phase space that produces a direct plunge is reduced if the MBH is rotating. The strongest spin effects appear with  $\theta = \pm 0.1$  rad and  $a_{\bullet} = 0.999$ ; in the case of prograde orbits,  $\hat{\theta}_{\mathcal{W}} \sim \hat{\theta}_K \sim 0.5 \hat{\theta}_S$ , and  $\hat{\theta}_{\mathcal{W}} \sim \hat{\theta}_K \sim 1.19 \hat{\theta}_S$  for  $\theta = -0.1$  rad.

Finally, we use Equations (10), (21), and (23) to solve Equation (19) with the correction factors embedded in the value of  $a_{\text{crit}}$ , thus obtaining

$$\dot{\Gamma}_i = \frac{3 - \beta}{2\lambda T_0} \frac{N_{\text{tot}}}{R_h^\lambda} f_{\text{sub}} \times \left\{ \left[ a_{\text{crit}}^\lambda \left( \ln \left( \frac{a_{\text{crit}}}{D} \right) - \frac{1}{\lambda} \right) \right] - \left[ a_{\text{min}}^\lambda \left( \ln \left( \frac{a_{\text{min}}}{D} \right) - \frac{1}{\lambda} \right) \right] \right\}, \quad (28)$$

with  $\lambda = (9/2) - \beta - \gamma$ , and  $D$  a term associated to the loss-cone angle, given by

$$D = \begin{cases} 8r_S, & \text{for } \hat{\theta}_{\text{lc}}^{-2} = \hat{\theta}_S^{-2}, \\ 8r_S \mathcal{W}(\theta, a_{\bullet}), & \text{for } \hat{\theta}_{\text{lc}}^{-2} = \hat{\theta}_{\mathcal{W}}^{-2}, \\ 0.5r_S [2 + 2K(\theta, a_{\bullet})]^2, & \text{for } \hat{\theta}_{\text{lc}}^{-2} = \hat{\theta}_K^{-2}. \end{cases} \quad (29)$$

## 5 EFFECT OF THE CORRECTION FACTORS AND THE LOSS-CONE ANGLE IN THE EVENT RATES

We consider systems composed of a central MBH of  $4.3 \times 10^6 M_{\odot}$  with a spin range  $a_{\bullet} = [0.0$ – $0.999]$  and an inspiraling object (a stellar-mass BH, an NS or a WD in the case of EMRIs; a BD in the case of X-MRIs) of mass  $m_2$ ; the masses and fraction numbers are given in Table 2. For the mass density distribution, we choose  $\gamma = 1.75$  for the stellar-mass BHs,  $\beta = 1.5$  for the lighter populations (Bahcall & Wolf 1976),  $R_h = 1$  pc, and  $N_0 = 1.2 \times 10^3$ .

Applying the correction factors results in longer merger time-scales compared to  $T_{\text{P}}$  and  $T_{\text{P}=0}$  (for high enough eccentricities), giving more time to the relaxation processes to perturb the orbit of the compact object and prevent an inspiral. Therefore, to decouple from the dynamics regime, the inspiraling body has to be closer to the MBH, resulting in a smaller critical semimajor axis such that  $a_{\text{RQ}} \lesssim a_{\text{P}=0} < a_{\text{P}}$ . The semimajor axis  $a_0$  of an inspiraling object would be

$a_{\bullet} = 0.0$				
Object	$e_{\min}$	$e_{\max}$		
BD	0.963178	0.998160		
WD	0.981957	0.999790		
NS	0.997268	0.999919		
BH	0.996791	0.999971		
$a_{\bullet} = 0.999$				
	Prograde		Retrograde	
	$e_{\min}$	$e_{\max}$	$e_{\min}$	$e_{\max}$
BD	0.990605	0.999954	0.947489	0.995773
WD	0.995396	0.999995	0.974270	0.999505
NS	0.999303	0.999998	0.996104	0.999810
BH	0.999181	0.999999	0.995424	0.999932

**Table 3.** Maximum and minimum eccentricity (Equations 30 and 31) for each type of compact object. The values of  $e_{\min}$  and  $e_{\max}$  are obtained for  $\theta = 0.1$  rad (prograde orbits),  $\theta = -0.1$  rad (retrograde orbits),  $a_{\text{crit}} = a_{\text{RQ}}$ ,  $M_{\text{MBH}} = 4.3 \times 10^6 M_{\odot}$ , and  $a_{\bullet} = 0$  or 0.999.

delimited by  $a_{\min}$  and  $a_{\text{crit}} < R_{\text{h}}$ , and the pericentre distance would be fixed at the LSO position (Equation 15). With these conditions, we define an eccentricity range  $e_0 = [e_{\min}(a_{\bullet}, \theta), e_{\max}(a_{\bullet}, \theta)]$  given by

$$e_{\max}(a_{\bullet}, \theta) = 1 - r_{\text{LSO}}/a_{\text{crit}}, \quad (30)$$

$$e_{\min}(a_{\bullet}, \theta) = 1 - r_{\text{LSO}}/a_{\min}. \quad (31)$$

Objects with  $e_0 > e_{\max}$  plunge into the MBH after a single pericentre passage, and as we do not expect to find objects with  $a_0 < a_{\min}$ , the value of  $e_{\min}$  defines the plunging limit for the objects that are located closest to the MBH.

As the pericentre is fixed, orbits with  $a_0 = a_{\dot{p}=0}$ , and specially with  $a_0 = a_{\text{P}}$  can have higher eccentricities than orbits with  $a_0 = a_{\text{RQ}}$ . For this reason, we obtain  $e_{\max}$  by setting  $a_{\text{crit}} = a_{\text{RQ}}$  in Equation (30); this eccentricity value is valid for all the cases, as  $a_{\text{crit}}$  sets the upper limit for the semi-major axis of an inspiraling orbit. Table 3 shows the range of eccentricities for the considered compact objects obtained for  $\theta = \pm 0.1$  rad,  $a_{\bullet} = [0.0, 0.999]$ , and  $a_{\text{crit}} = a_{\text{RQ}}$ .

### 5.1 The effect of the correction factors

To investigate the effect of the correction factors in the inspiraling rates, we estimate  $\dot{\Gamma}_i$  with  $\hat{\theta}_{\text{lc}} = \hat{\theta}_{\text{S}}$  in the eccentricity range given by Equations (30) and (31). We denote as  $\dot{\Gamma}_{\text{P}}$  the event rates without the corrections, i.e. setting  $RQ = 1$  in Equation (28), as  $\dot{\Gamma}_{\text{RQ}}$  the rates with the correction factors included, and as  $\dot{\Gamma}_{\dot{p}=0}$  the event rates computed as in Amaro-Seoane et al. (2013), where Equation (3) is used as merger time-scale.

For the initial eccentricities given in Table 3, the correction factor  $R$  (Equation 4) takes a value that goes from  $R \sim 5$  when  $e_0 \sim 0.94$ , to  $\sim 8$  when  $e \rightarrow 1$ . The factor  $Q$  (Equations 16 and 17) is mainly affected by the spin and the orbital inclination; for a fixed  $\theta$ , the PN correction reaches its maximum value when  $a_{\bullet} = 0.999$ .

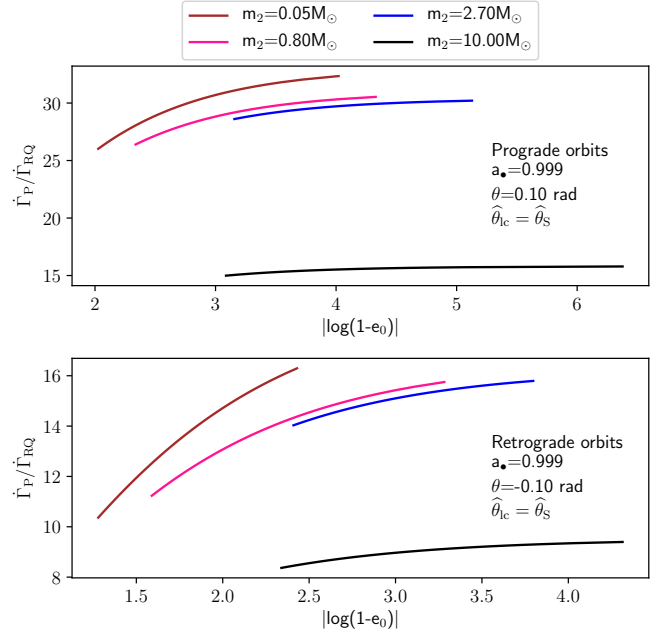


**Figure 4.** Ratio  $\dot{\Gamma}_{\text{P}}/\dot{\Gamma}_{\text{RQ}}$  as a function of the initial eccentricity for EMRIs and X-MRIs in orbits with  $\theta = 0.1$  rad (upper panel) and  $\theta = -0.1$  rad (lower panel) around a  $4.3 \times 10^6 M_{\odot}$  Kerr MBH with  $a_{\bullet} = 0.999$ .  $\dot{\Gamma}_{\text{P}}$  represents the event rates obtained using Peters' formula as the merger time-scale (i.e. setting  $RQ = 1$  in Equation 28), whereas  $\dot{\Gamma}_{\text{RQ}}$  are the corrected values. Both event rates are obtained with the usual loss-cone angle  $\hat{\theta}_{\text{S}}$ . Brown lines represent a BD ( $m_2 = 0.05 M_{\odot}$ ) X-MRI, blue lines an inspiraling NS ( $m_2 = 2.7 M_{\odot}$ ) EMRI, pink lines a WD ( $m_2 = 0.8 M_{\odot}$ ) EMRI, and black lines a stellar-mass BH ( $m_2 = 10 M_{\odot}$ ) EMRI.

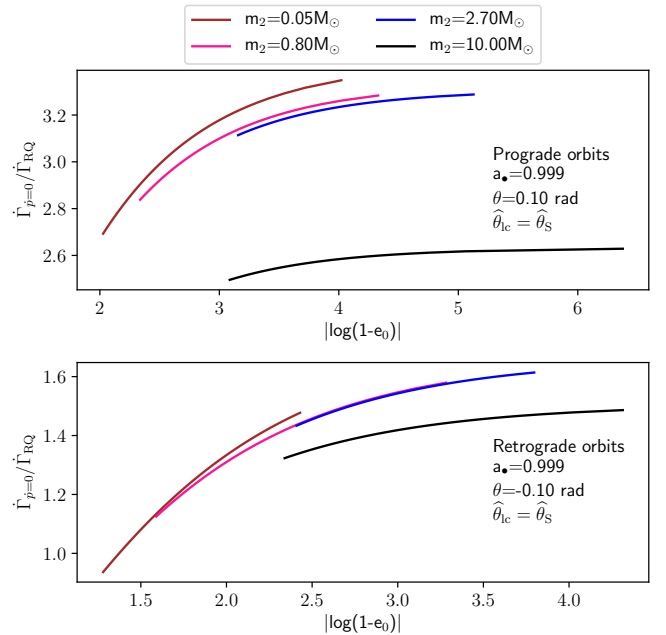


**Figure 5.** Same as Figure 4, but for the ratio  $\dot{\Gamma}_{\dot{p}=0}/\dot{\Gamma}_{\text{RQ}}$ . The rates  $\dot{\Gamma}_{\dot{p}=0}$  are obtained using Equation (3) as the merger time-scale.



$a_\bullet = 0.0$	$\dot{\Gamma}_P/\dot{\Gamma}_{\text{RQ}}$		$\dot{\Gamma}_{\dot{p}=0}/\dot{\Gamma}_{\text{RQ}}$	
	$e_{\text{min}}$	$e_{\text{max}}$	$e_{\text{min}}$	$e_{\text{max}}$
BD	14.429	21.712	1.364	2.057
WD	15.319	20.628	1.566	2.110
NS	18.360	20.408	1.913	2.127
BH	10.436	11.500	1.675	1.846

$a_\bullet = 0.999$	$\dot{\Gamma}_P/\dot{\Gamma}_{\text{RQ}}$			
	$\theta = 0.1 \text{ rad}$		$\theta = -0.1 \text{ rad}$	
	$e_{\text{min}}$	$e_{\text{max}}$	$e_{\text{min}}$	$e_{\text{max}}$
BD	26.021	32.344	10.365	16.295
WD	26.396	30.533	11.234	15.751
NS	28.609	30.205	14.031	15.794
BH	14.990	15.788	8.366	9.396

$a_\bullet = 0.999$	$\dot{\Gamma}_{\dot{p}=0}/\dot{\Gamma}_{\text{RQ}}$			
	$\theta = 0.1 \text{ rad}$		$\theta = -0.1 \text{ rad}$	
	$e_{\text{min}}$	$e_{\text{max}}$	$e_{\text{min}}$	$e_{\text{max}}$
BD	2.693	3.349	0.936	1.477
WD	2.838	3.283	1.125	1.579
NS	3.114	3.288	1.433	1.614
BH	2.496	2.629	1.323	1.486

**Table 4.** Ratios  $\dot{\Gamma}_P/\dot{\Gamma}_{\text{RQ}}$  and  $\dot{\Gamma}_{\dot{p}=0}/\dot{\Gamma}_{\text{RQ}}$  for EMRIs and X-MRIs with  $\theta = \pm 0.1$  rad, around an MBH of mass  $M_{\text{MBH}} = 4.3 \times 10^6 M_\odot$ , and  $a_\bullet = 0$  or 0.999.

Figures 4 and 5 show the ratios  $\dot{\Gamma}_P/\dot{\Gamma}_{\text{RQ}}$  and  $\dot{\Gamma}_{\dot{p}=0}/\dot{\Gamma}_{\text{RQ}}$ , respectively, as a function of the initial eccentricity for the considered EMRIs and X-MRIs in prograde and retrograde orbits with  $\theta = \pm 0.1$  rad,  $\hat{\theta}_{\text{lc}} = \hat{\theta}_S$ , and  $a_\bullet = 0.999$ . These plots show the largest difference between the rates, as this configuration of MBH spin and orbital inclinations results in the highest (lowest) event rates in the case of prograde (retrograde) orbits. As shown in Table 4, the combined effect of the eccentricity evolution and the PN corrections represents an important improvement over  $\dot{\Gamma}_P$ : for a central MBH with  $a_\bullet = 0.999$ ,  $\dot{\Gamma}_P \sim 8 - 30 \dot{\Gamma}_{\text{RQ}}$ ; for  $a_\bullet = 0$ ,  $\dot{\Gamma}_P \sim 10 - 20 \dot{\Gamma}_{\text{RQ}}$ . On the other hand, the estimate given by  $\dot{\Gamma}_{\dot{p}=0}$  is between  $\sim 1.3$  and 2 times larger than the fully corrected value  $\dot{\Gamma}_{\text{RQ}}$  when  $a_\bullet = 0$ , and between  $\dot{\Gamma}_{\dot{p}=0} \sim 0.9 - 3 \dot{\Gamma}_{\text{RQ}}$  for  $a_\bullet = 0.999$ .

To show the effect of the spin on  $\dot{\Gamma}_{\dot{p}=0}$  and  $\dot{\Gamma}_{\text{RQ}}$ , we compute event rates considering  $a_\bullet = 0$  and  $a_\bullet = 0.999$ . For a central MBH ( $M_{\text{MBH}} = 4.3 \times 10^6 M_\odot$ ) with  $a_\bullet = 0$ , we obtain  $\dot{\Gamma}_i^{\text{Schw}} \sim 10^{-6} - 10^{-7} \text{ yr}^{-1}$  for the considered EMRIs and X-MRIs. However, the event rates denoted as  $\dot{\Gamma}_i^{\text{Kerr}}$  for  $a_\bullet \neq 0$ , are higher than  $\dot{\Gamma}_i^{\text{Schw}}$  when the inspiraling orbits are prograde, and  $\dot{\Gamma}_i^{\text{Kerr}} \lesssim \dot{\Gamma}_i^{\text{Schw}}$  if the orbits are retrograde. For  $\theta = 0.1$  rad, the rates  $\dot{\Gamma}_i^{\text{Kerr}}$  are enhanced by a factor that can be as high as  $\sim 47$  with respect to  $\dot{\Gamma}_{\dot{p}=0}^{\text{Schw}}$ . With the correction factors, we obtain that  $\dot{\Gamma}_{\text{RQ}}^{\text{Kerr}}$  increases by a factor  $\sim 23$  with respect to  $\dot{\Gamma}_{\text{RQ}}^{\text{Schw}}$  in the most extreme case ( $a_\bullet = 0.999$ ,

	$\dot{\Gamma}_{\text{RQ}}^{\text{Kerr}}/\dot{\Gamma}_{\text{RQ}}^{\text{Schw}}$	$\dot{\Gamma}_{\dot{p}=0}^{\text{Kerr}}/\dot{\Gamma}_{\dot{p}=0}^{\text{Schw}}$
$\theta = 0.1 \text{ rad}$		
BD	23.841	47.071
WD	23.068	41.817
NS	24.807	40.378
BH	13.371	19.92
$\theta = -0.1 \text{ rad}$		
BD	0.509	0.350
WD	0.515	0.370
NS	0.500	0.375
BH	0.573	0.452

**Table 5.** Ratios  $\dot{\Gamma}_{\text{RQ}}^{\text{Kerr}}/\dot{\Gamma}_{\text{RQ}}^{\text{Schw}}$  and  $\dot{\Gamma}_{\dot{p}=0}^{\text{Kerr}}/\dot{\Gamma}_{\dot{p}=0}^{\text{Schw}}$  obtained for WD, NS, and BH EMRIs, and a BD X-MRI in prograde and retrograde orbits, with  $|\theta| = 0.1$  rad, around a central MBH with mass  $M_{\text{MBH}} = 4.3 \times 10^6 M_\odot$ , and a spin value of  $a_\bullet = 0.999$  in the Kerr case.

$\theta = 0.1$  rad). In Table 5, we show the ratios  $\dot{\Gamma}_{\dot{p}=0}^{\text{Kerr}}/\dot{\Gamma}_{\dot{p}=0}^{\text{Schw}}$  and  $\dot{\Gamma}_{\text{RQ}}^{\text{Kerr}}/\dot{\Gamma}_{\text{RQ}}^{\text{Schw}}$ .

We choose the specific case of a BH EMRI approaching a central MBH ( $M_{\text{MBH}} = 4.3 \times 10^6 M_\odot$ ) in an orbit with  $e_0 = 0.9992$  to show the influence of the spin and the orbital inclination. Figure 6 shows the ratio  $\dot{\Gamma}_{\dot{p}=0}/\dot{\Gamma}_{\text{RQ}}$  for this EMRI as a function of  $a_\bullet$ , obtained with different orbital inclinations ( $\theta = [0, \pm 0.1, \pm 0.4, \pm 0.7, \pm 1.0, \pm 1.3, \pm 1.57]$  rad). In the prograde cases, the difference between  $\dot{\Gamma}_{\text{RQ}}$  and  $\dot{\Gamma}_{\dot{p}=0}$  is larger for high spin values because the LSO shifts closer to the event horizon, and relativistic effects become more important. On the contrary, relativistic effects are weaker for retrograde orbits, as the LSO is pushed away from the event horizon.

Finally, for the eccentricity range given in Table 3, we plot in Figure 7 the rates  $\dot{\Gamma}_{\text{RQ}}$  and  $\dot{\Gamma}_{\dot{p}=0}$  for objects with orbital inclinations  $\theta = \pm 0.1$  rad approaching a Kerr MBH of mass  $M_{\text{MBH}} = 4.3 \times 10^6 M_\odot$  and  $a_\bullet = 0.999$ . Prograde WD EMRIs have the highest event rates with  $\dot{\Gamma}_{\dot{p}=0} \sim 1.5 \times 10^{-4} \text{ yr}^{-1}$  and  $\dot{\Gamma}_{\text{RQ}} \sim 5 \times 10^{-5} \text{ yr}^{-1}$ . For NS EMRIs we obtain  $\dot{\Gamma}_{\dot{p}=0} \sim 3.2 \times 10^{-5} \text{ yr}^{-1}$ , and  $\dot{\Gamma}_{\dot{p}=0} \gtrsim 2 \times 10^{-5} \text{ yr}^{-1}$  for BH EMRIs, and BD X-MRIs. The corrected version gives  $\dot{\Gamma}_{\text{RQ}} \sim 1 \times 10^{-5} \text{ yr}^{-1}$  for NS EMRIs,  $\dot{\Gamma}_{\text{RQ}} \gtrsim 9 \times 10^{-6} \text{ yr}^{-1}$  for BH EMRIs, and  $\dot{\Gamma}_{\text{RQ}} \sim 6.5 - 8 \times 10^{-6} \text{ yr}^{-1}$  for BD X-MRIs.

The highest event rate of the retrograde cases is also obtained for WD EMRIs with  $\dot{\Gamma}_{\dot{p}=0} \sim 1.4 \times 10^{-6} \text{ yr}^{-1}$  and  $\dot{\Gamma}_{\text{RQ}} \sim 1.2 \times 10^{-6} - 8.6 \times 10^{-7} \text{ yr}^{-1}$ . For retrograde BH EMRIs, NS EMRIs, and BD X-MRIs the event rates are  $\sim 10^{-7} \text{ yr}^{-1}$ , and  $\dot{\Gamma}_{\text{RQ}} \lesssim \dot{\Gamma}_{\dot{p}=0}$ , with the only exception occurring at  $e_0 \lesssim 0.95$ , where  $\dot{\Gamma}_{\dot{p}=0} \lesssim \dot{\Gamma}_{\text{RQ}}$  for BD X-MRIs. These values remain approximately constant along the eccentricity range, the largest variation occurring for retrograde BD X-MRIs, where there is a difference of a factor  $\sim 1.5$  between the values of  $\dot{\Gamma}_{\text{RQ}}$  evaluated at  $e_{\text{min}}$  and  $e_{\text{max}}$ .

Note that  $\dot{\Gamma}_{\text{RQ}}$  gives an upper limit for the event rate when  $\theta = 0.1$  rad, because  $p_0 < 3r_S$  and the correction factor  $Q$  is evaluated at  $p_0 = 3r_S$ , whereas for  $\theta = -0.1$  rad  $\dot{\Gamma}_{\text{RQ}}$  contains the full PN correction as  $p_0 > 3r_S$ .

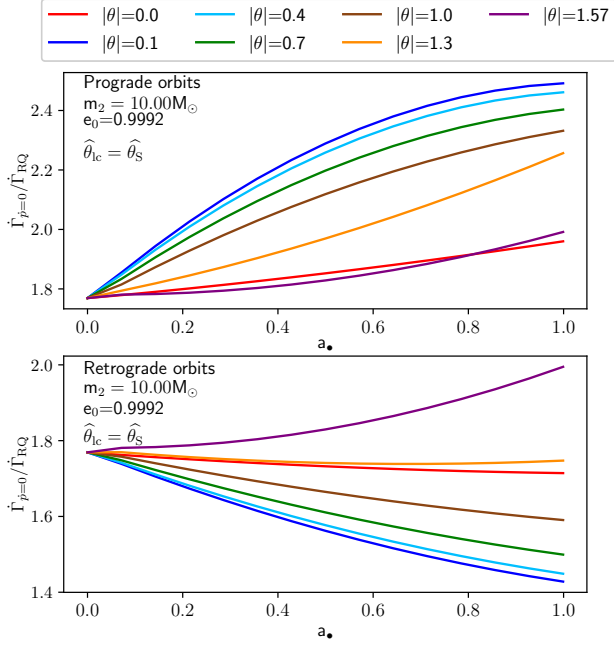


**Figure 6.** Ratio  $\dot{\Gamma}_{\dot{p}=0}/\dot{\Gamma}_{\text{RQ}}$  as a function of the spin  $a_\bullet$  for a BH EMRI approaching a central MBH of mass  $M_{\text{MBH}} = 4.3 \times 10^6 M_\odot$ . The colors represent the different orbital inclinations,  $\theta$ , given in radians. The top (bottom) panel shows the prograde (retrograde) cases.

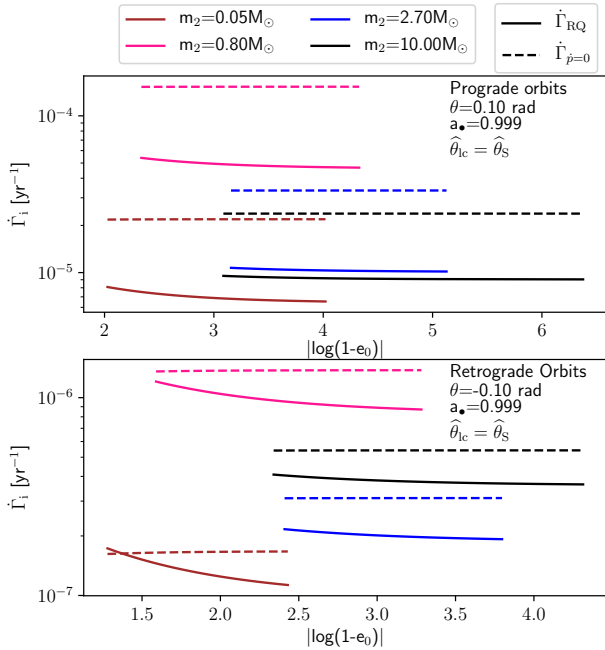


**Figure 7.** Inspiral event rates for prograde (upper panel) and retrograde orbits (lower panel) with  $|\theta| = 0.1$  rad, around a central MBH ( $M_{\text{MBH}} = 4.3 \times 10^6 M_\odot$ ) with  $a_\bullet = 0.999$ ;  $\dot{\Gamma}_{\dot{p}=0}$  (dotted lines) is obtained with the time-scale  $T_{\dot{p}=0}$  (Equation 3), whereas  $\dot{\Gamma}_{\text{RQ}}$  (solid lines) comes from Equation (28). Brown lines represent a BD ( $m_2 = 0.05 M_\odot$ ) X-MRI, blue lines an NS ( $m_2 = 2.7 M_\odot$ ) EMRI, pink lines a WD ( $m_2 = 0.8 M_\odot$ ) EMRI, and black lines a stellar-mass BH ( $m_2 = 10 M_\odot$ ) EMRI.

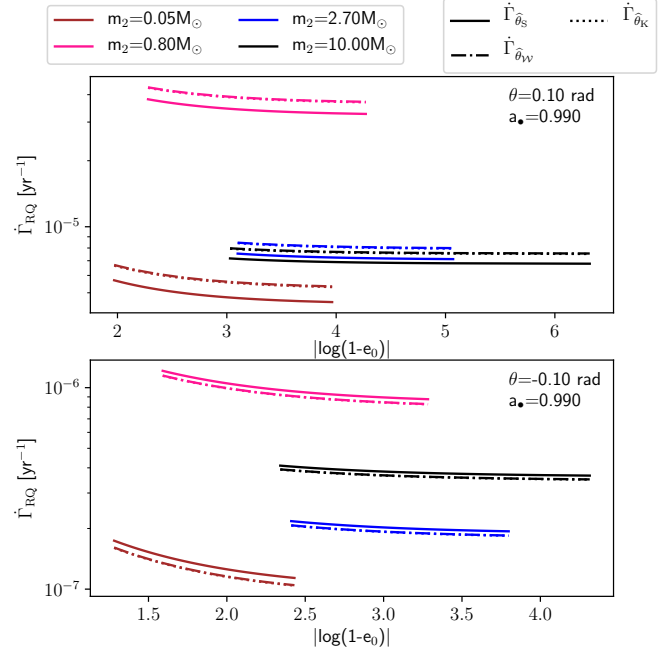


**Figure 8.** Event rates  $\dot{\Gamma}_{\text{RQ}}$  computed with the different loss-cone angles, as a function of  $e_0$  for EMRIs and X-MRIs with  $|\theta| = 0.1$  rad in prograde (upper panel), and retrograde orbits (lower panel), around a MBH of mass  $M_{\text{MBH}} = 4.3 \times 10^6 M_\odot$ , and  $a_\bullet = 0.99$ . The subscript indicates which loss-cone angle is used to obtain the event rates;  $\hat{\theta}_{\text{S}}$  is given by Equation (24),  $\hat{\theta}_{\text{W}}$  is the Kerr loss-cone angle given by Equation (25), and  $\hat{\theta}_{\text{K}}$  is given by Equation (27).

## 5.2 The effect of the loss-cone angle

The shift in the LSO position can reduce or increase the magnitude of the loss-cone angle, modifying the phase-space volume that places the pericentre of an orbit inside the LSO. As  $a_\bullet \rightarrow 1$ , the Kerr loss-cone angles  $\hat{\theta}_{\text{W}}$  and  $\hat{\theta}_{\text{K}}$  (Equations 25 and 27) deviate more from the Schwarzschild loss-cone angle  $\hat{\theta}_{\text{S}}$ . However, the change in the event rates is small even for high spin values, as  $\dot{\Gamma}_i \propto \ln(\hat{\theta}_{\text{lc}}^{-2})$ .

The factor  $Q$  indicates that the influence of  $a_\bullet$  and  $\theta$  is not as large as the one obtained when the function  $\mathcal{W}(\theta, a_\bullet)$  is implemented (see Table 5), so it is no surprise that the rates  $\dot{\Gamma}_{\dot{p}=0}$  are more affected by  $\hat{\theta}_{\text{W}}$  and  $\hat{\theta}_{\text{K}}$  compared to  $\dot{\Gamma}_{\text{RQ}}$ .

By computing  $\dot{\Gamma}_{\text{RQ}}$  and  $\dot{\Gamma}_{\dot{p}=0}$  with  $\hat{\theta}_{\text{lc}} = \hat{\theta}_{\text{S}}$ ,  $\hat{\theta}_{\text{W}}$ , and  $\hat{\theta}_{\text{K}}$  for a spin value of  $a_\bullet = 0.99$  that guarantees the accuracy within 5 per cent of  $J_{\text{crit}}$  (Equation 26), we find that the asymmetric effect of the MBH spin is still noticeable. It can be seen in Figure 8, where we show the corrected event rates computed with the different loss-cone angles –  $\hat{\Gamma}_{\hat{\theta}_{\text{S}}}$ ,  $\hat{\Gamma}_{\hat{\theta}_{\text{W}}}$ , and  $\hat{\Gamma}_{\hat{\theta}_{\text{K}}}$  – as a function of  $e_0$  for the considered EMRIs and X-MRIs.

In Section 4.2, we showed that, for prograde orbits around a Kerr MBH,  $\hat{\theta}_{\text{W}} \sim \hat{\theta}_{\text{K}}$ , and that, for high spin values,  $\hat{\theta}_{\text{W}} \lesssim 0.5 \hat{\theta}_{\text{S}}$ . This reduction in the loss-cone angle increases the EMRI and X-MRI event rates  $\dot{\Gamma}_{\dot{p}=0}$  by a factor  $\sim 1.2$  compared to the Schwarzschild case. For objects in retrograde orbits,  $\dot{\Gamma}_{\dot{p}=0}$  are reduced by a factor  $\sim 0.8$  due to the small increase in the magnitude of the Kerr loss-cone angle. In the case of  $\dot{\Gamma}_{\text{RQ}}$ , the Kerr loss-cone angle changes the rates estimate by a factor  $\sim 0.9$  to  $\sim 1.1$ , which is still negligible. In Table 6, we give the ratio between these rates.

$\dot{\Gamma}_{\text{RQ}}$	$\dot{\Gamma}_{\hat{\theta}_{\text{W}}}/\dot{\Gamma}_{\hat{\theta}_{\text{S}}}$		$\dot{\Gamma}_{\hat{\theta}_{\text{K}}}/\dot{\Gamma}_{\hat{\theta}_{\text{S}}}$	
$\theta$ [rad]	0.1	-0.1	0.1	-0.1
BD	1.17	0.92	1.16	0.92
WD	1.13	0.94	1.12	0.94
NS	1.12	0.95	1.11	0.95
BH	1.11	0.95	1.10	0.95

$\dot{\Gamma}_{\dot{p}=0}$	$\dot{\Gamma}_{\hat{\theta}_{\text{W}}}/\dot{\Gamma}_{\hat{\theta}_{\text{S}}}$		$\dot{\Gamma}_{\hat{\theta}_{\text{K}}}/\dot{\Gamma}_{\hat{\theta}_{\text{S}}}$	
$\theta$ [rad]	0.1	-0.1	0.1	-0.1
BD	1.22	0.89	1.21	0.88
WD	1.16	0.93	1.15	0.92
NS	1.14	0.94	1.13	0.93
BH	1.13	0.94	1.12	0.94

**Table 6.** Comparison of event rates computed with  $\hat{\theta}_{\text{S}}$  and the Kerr loss-cone angles  $\hat{\theta}_{\text{W}}$  and  $\hat{\theta}_{\text{K}}$  for each inspiraling object. We take  $\theta = \pm 0.1$  rad,  $M_{\text{MBH}} = 4.3 \times 10^6 M_{\odot}$ , and  $\mathbf{a}_{\bullet} = 0.99$ . The upper section shows the change induced by the Kerr loss-cone angles in  $\dot{\Gamma}_{\text{RQ}}$  and the lower part shows the change in  $\dot{\Gamma}_{\dot{p}=0}$ .

## 6 DISCUSSION AND CONCLUSIONS

The spin of the MBH and the orbital inclination of the inspiraling object can not be ignored; these quantities can affect the event rates in two forms. Firstly, through the pericentre of an inspiraling orbit: as we fix the pericentre at  $r_{\text{LSO}}$ , a shift in the LSO position changes the value of the critical semimajor axis and the integration volume of Equation (19), significantly enhancing the event rates of prograde orbits, and slightly reducing the event rates in the retrograde cases, as the effect of the MBH spin is not symmetric. Secondly, through the loss-cone: its value also depends on  $r_{\text{LSO}}$  and determines the set of velocity vectors that take an object to a direct plunge. We give two expressions,  $\hat{\theta}_{\text{W}}$  and  $\hat{\theta}_{\text{K}}$ , to obtain a loss-cone angle that accounts for spin effects. Both versions of the Kerr loss-cone angle give similar results and, as  $\mathbf{a}_{\bullet} \rightarrow 1$ ,  $\hat{\theta}_{\text{W}}$  and  $\hat{\theta}_{\text{K}}$  deviate more from the Schwarzschild case  $\hat{\theta}_{\text{S}}$ . However, we find that the influence of the MBH spin added through the pericentre condition,  $p_0 = r_{\text{LSO}}$ , already contains the most relevant effects regarding the event rates, so that implementing  $\hat{\theta}_{\text{W}}$  or  $\hat{\theta}_{\text{K}}$  changes the event rates by a factor that ranges between 0.9 and 1.2, which does not produce a significant impact on the rate estimates.

We obtained event rates for EMRIs and X-MRIs by implementing three different merger time-scales,  $T_{\text{P}}$ ,  $T_{\text{RQ}}$ , and  $T_{\dot{p}=0}$ . Peters' formula,  $T_{\text{P}}$ , overestimates the energy loss by GWs and fails to give an accurate merger time-scale; this can be avoided by including eccentricity evolution and post-Newtonian corrections through the correction factors  $R$  and  $Q$ ; the resulting time-scale,  $T_{\text{RQ}}$ , is longer than  $T_{\text{P}}$  and produces the best merger time-scale estimate for arbitrary eccentricities, orbital inclinations, and MBH spin values. The alternative formulation  $T_{\dot{p}=0}$  gives a good estimate of the merger time-scale,  $T_{\dot{p}=0} \lesssim T_{\text{RQ}}$ , in the context of EMRIs and X-MRIs. However, for arbitrary values of  $e_0$ ,  $\theta$ , or  $\mathbf{a}_{\bullet}$ , its accuracy can not be guaranteed.

We have shown that for the eccentricity range and pericentre distances expected for EMRIs and X-MRIs ( $e_0 > 0.9$ ,  $p_0 = r_{\text{LSO}}$ ), implementing  $T_{\text{GW}} = T_{\text{P}}$  results in unreliable event rates estimates.  $\dot{\Gamma}_{\text{P}}$  are artificially enhanced by a factor that ranges between  $\sim 8$  to 30 compared to the corrected values  $\dot{\Gamma}_{\text{RQ}}$ . On the other hand, the estimates given by  $\dot{\Gamma}_{\dot{p}=0}$ , which include the influence of the MBH spin and the orbital inclination through the function  $\mathcal{W}(\theta, \mathbf{a}_{\bullet})$ , differ from  $\dot{\Gamma}_{\text{RQ}}$  by a factor between 0.9 and 3.

We conclude that both the Kerr loss-cone and the  $RQ$  corrections to Peters' time-scale do not have a dramatic impact on the event rates for EMRIs or X-MRIs, when compared to the high-eccentricity approach of Amaro-Seoane et al. (2013). However, this work considers only the dynamical and relativistic aspects of the EMRIs and X-MRIs formation and considers the galactic nucleus of the Milky Way as a representative example of the galaxies that could harbour potential inspiral sources. If EMRIs and X-MRIs in Nature happened to form at very low eccentricities, or if environmental effects (not included in this work; e.g. torques induced by background gas) can induce a significant reduction of the initial eccentricity of EMRIs and X-MRIs ( $e_0 \lesssim 0.8$ ), it would be necessary to implement the eccentricity-evolution and PN corrections to obtain accurate event rate estimates. In any case, all event rates for MBH binaries and stellar-mass binaries should be revisited using our improvements because their eccentricities will span through all possible values.

## ACKNOWLEDGMENTS

PAS acknowledges support from the Ramón y Cajal Programme of the Ministry of Economy, Industry and Competitiveness of Spain, as well as the financial support of Programa Estatal de Generación de Conocimiento (ref. PGC2018-096663-B-C43) (MCIU/FEDER). This work was supported by the National Key R&D Program of China (2016YFA0400702) and the National Science Foundation of China (11721303, 11873022 and 11991053). PRC, LM, and LZ acknowledge support from the Swiss National Science Foundation under the Grant 200020\_178949. EB acknowledges support from the European Research Council (ERC) under the European Union's Horizon 2020 research and innovation program ERC-2018-COG under grant agreement N. 818691 (B Massive).

## DATA AVAILABILITY STATEMENT

The data underlying this article will be shared on reasonable request to the corresponding author.

## REFERENCES

- Alexander T., Hopman C., 2003, *ApJ*, **590**, L29
- Alexander T., Hopman C., 2009, *ApJ*, **697**, 1861
- Amaro-Seoane P., 2018, *Living Reviews in Relativity*, **21**, 4
- Amaro-Seoane P., 2019, *Phys. Rev. D*, **99**, 123025
- Amaro-Seoane P., 2020, The gravitational capture of compact objects by massive black holes ([arXiv:2011.03059](https://arxiv.org/abs/2011.03059))

- Amaro-Seoane P., Preto M., 2011, *Classical and Quantum Gravity*, **28**, 094017
- Amaro-Seoane P., Freitag M., Spurzem R., 2004, *Monthly Notices of the Royal Astronomical Society*, **352**, 655–672
- Amaro-Seoane P., Gair J. R., Freitag M., Miller M. C., Mandel I., Cutler C. J., Babak S., 2007, *Classical and Quantum Gravity*, **24**, 113
- Amaro-Seoane P., et al., 2012, *Classical and Quantum Gravity*, **29**, 124016
- Amaro-Seoane P., Sopuerta C. F., Freitag M. D., 2013, *MNRAS*, **429**, 3155
- Babak S., et al., 2017, *Phys. Rev. D*, **95**, 103012
- Bahcall J. N., Wolf R. A., 1976, *ApJ*, **209**, 214
- Barack L., Cutler C., 2004, *Phys. Rev. D*, **69**, 082005
- Barack L., et al., 2019, *Classical and Quantum Gravity*, **36**, 143001
- Baumgardt H., Makino J., Ebisuzaki T., 2004a, *ApJ*, **613**, 1133
- Baumgardt H., Makino J., Ebisuzaki T., 2004b, *ApJ*, **613**, 1143
- Baumgardt H., Amaro-Seoane P., Schödel R., 2018, *A&A*, **609**, A28
- Binney J., Tremaine S., 1987, *Galactic dynamics*. Princeton Univ. Press
- Bonetti M., Perego A., Capelo P. R., Dotti M., Miller M. C., 2018, *Publ. Astron. Soc. Australia*, **35**, e017
- Brown W. R., Geller M. J., Kenyon S. J., Kurtz M. J., 2005, *ApJ*, **622**, L33
- Einstein A., 1916, *Annalen der Physik*, **354**, 769
- Freitag M., Benz W., 2001, *A&A*, **375**, 711
- Freitag M., Benz W., 2002, *A&A*, **394**, 345
- Freitag M., Amaro-Seoane P., Kalogera V., 2006, in *Journal of Physics Conference Series*. pp 252–258 ([arXiv:astro-ph/0607001](https://arxiv.org/abs/astro-ph/0607001)), doi:10.1088/1742-6596/54/1/040
- Gallego-Cano E., Schödel R., Dong H., Nogueras-Lara F., Gallego-Calvente A. T., Amaro-Seoane P., Baumgardt H., 2018, *A&A*, **609**, A26
- Hills J. G., 1988, *Nature*, **331**, 687
- Hopman C., Alexander T., 2005, *ApJ*, **629**, 362
- Kerr R. P., 1963, *Phys. Rev. Lett.*, **11**, 237
- Klein A., et al., 2016, *Phys. Rev. D*, **93**, 024003
- Kroupa P., 2001, *MNRAS*, **322**, 231
- Merritt D., 2013, *Classical and Quantum Gravity*, **30**, 244005
- Peebles P. J. E., 1972, *ApJ*, **178**, 371
- Peters P. C., 1964, PhD thesis, California Institute of Technology
- Peters P. C., Mathews J., 1963, *Physical Review*, **131**, 435
- Preto M., Amaro-Seoane P., 2009, *The Astrophysical Journal*, **708**, L42
- Schödel R., Gallego-Cano E., Dong H., Nogueras-Lara F., Gallego-Calvente A. T., Amaro-Seoane P., Baumgardt H., 2018, *A&A*, **609**, A27
- Schwarzschild K., 1916, *Abh. Konigl. Preuss. Akad. Wissenschaften Jahre 1906,92*, Berlin,1907, **1916**, 189
- Sigurdsson S., Rees M. J., 1997, *MNRAS*, **284**, 318
- Sopuerta C. F., Yunes N., 2011, *Physical Review D*, **84**
- Teukolsky S., Shapiro S., 1983, *Black holes, white dwarfs, and neutron stars : the physics of compact objects*. Wiley
- Will C. M., 2012, *Classical and Quantum Gravity*, **29**, 217001
- Zwick L., Capelo P. R., Bortolas E., Mayer L., Amaro-Seoane P., 2020, *MNRAS*, **495**, 2321
- Zwick L., Capelo P. R., Bortolas E., Vázquez-Aceves V., Mayer L., Amaro-Seoane P., 2021, *MNRAS*, **506**, 1007

This paper has been typeset from a  $\text{\TeX}/\text{\LaTeX}$  file prepared by the author.